



Article

Channel Activity Remote Sensing Retrieval Model: A Case Study of the Lower Yellow River

Taixia Wu ^{1,†}, Zenan Xu ^{1,†}, Ran Chen ¹, Shudong Wang ^{2,3,*} and Tao Li ⁴

¹ School of Earth Sciences and Engineering, Hohai University, Nanjing 211100, China; wutx@hhu.edu.cn (T.W.); zn335889862@163.com (Z.X.)

² Aerospace Information Research Institute, Chinese Academy of Sciences, Haidian District, Beijing 100094, China

³ Collaborative Innovation Center on Forecast and Evaluation of Meteorological Disasters (CIC-FEMD), Nanjing University of Information Science & Technology, Nanjing 210044, China

⁴ The Shijin Irrigation District Affairs Center, Hebei Water Affairs Center, Shijiazhuang 050000, China

* Correspondence: wangsd@radi.ac.cn

† These authors contributed equally to this work.

Abstract: Meandering channel migration is a widespread phenomenon in rivers all around the world. Channel activity, which reflects the rate of change of a meandering channel, is calculated by averaging lateral channel migration. Channel migration can create new channels and abandon old ones, with effects on the natural environment. Floods can even lead to excessive rates of channel migration, which can threaten cities or farmland. Remote sensing can detect the spatial and temporal dynamic characteristics of the river channel, taking into account both spatial and temporal resolution, and can help in planning for the safety of the river channel in advance. Previous studies on river channels have suffered from a low accuracy of data, low level of automation, and subjectivity. To overcome these limitations, we propose a channel activity remote sensing retrieval model (CARSM) in this paper. CARSM extracts water using the modified normalized difference water index (MNDWI) combined with Otsu's method on the Google Earth Engine (GEE) platform, then extracts the channel centerlines via water mask maps using RivWidthCloud, and finally calculates channel activity based on the geometric relationship of the channel centerlines. With more objective extraction results, CARSM can guarantee more than 95% accuracy of channel activity and its high degree of automation can save a lot of labor costs. We use Landsat images to monitor the channel of the Lower Yellow River and calculate the overall and segmental channel activity separately. Our results show that the overall channel activity of the Lower Yellow River has gradually decreased between 1990 and 2020, with decreases of 33.04% and 41.06%, respectively. Analysis of channel activity reveals that the water sediment pattern of the Lower Yellow River changed from siltation to scouring after the completion of Xiaolangdi Reservoir, and the Lower Yellow River is gradually becoming stable.

Keywords: channel activity; water index; channel centerline; Lower Yellow River



Citation: Wu, T.; Xu, Z.; Chen, R.; Wang, S.; Li, T. Channel Activity Remote Sensing Retrieval Model: A Case Study of the Lower Yellow River. *Remote Sens.* **2023**, *15*, 3636. <https://doi.org/10.3390/rs15143636>

Academic Editor: Renato Frasson

Received: 17 June 2023

Revised: 11 July 2023

Accepted: 20 July 2023

Published: 21 July 2023



Copyright: © 2023 by the authors. Licensee MDPI, Basel, Switzerland. This article is an open access article distributed under the terms and conditions of the Creative Commons Attribution (CC BY) license (<https://creativecommons.org/licenses/by/4.0/>).

1. Introduction

Channel migration is a geomorphic process of alluvial rivers and is often used to describe the geometric changes of meandering flows [1–5]. Alluvial rivers consist of extensive one-way channels and exhibit planar patterns of varying curvature. Alluvial rivers erode banks and deposit sediment, causing the channel to migrate over the floodplain [6–9], and it will change its natural migration rule under human interference [10,11]. The migration rate of the river channel is usually described quantitatively through lateral migration or channel activity [12–17]. Lateral migration statistics tend to count migration on bends in the river, while channel activity statistics are for the entire river or sub-channel. Channel activity, defined as the average rate of lateral migration along a river channel per unit time [10,13,18], has been widely used in various river studies. River channel migration

may change the flow path of the river itself, such as straightening the bend to create an oxbow lake, or truncating the bend to create an abandoned river, thus affecting the natural ecological environment. High channel migration rates and river instability may lead to loss of farmland or villages and damage to riverbank embankments [17,19–22]. River channels change frequently and are closely related to human beings and the natural environment. Therefore, it is necessary to monitor the rate and status of river channel migrations and plan ahead for future channel improvement. However, repeated measurements of channel activity and its changes over time require a lot of human and financial costs, and the use of remote sensing has greatly reduced this human cost input [2,6]. Therefore, using remote sensing satellite images to efficiently extract information on morphological changes of river channels in space and time has some advantages in monitoring the activity of river channels.

The study of channel activity, which includes theoretical analysis of channel migrations at temporal and spatial scales as well as empirical investigation of changes to understand the specific causes of channel migrations, has been well-investigated by many researchers [23–27]. Using digital maps and aerial images of the centerline of the river channel under before-and-after coverage and calculating the channel activity in bends and intervals, Shields Jr. et al. [10] concludes that reservoir construction and flow regulation are important factors in reducing channel activity, while channel activity is only weakly correlated with the geometric characteristics of bend morphology. Using historical maps, aerial photographs or other historical documents, Magdaleno and Fernández-Yuste [18] analyzed the spatial and temporal evolution of the main geomorphic parameters of the central free-bend section of the Ebro River, Spain, between 1927 and 2003, and concluded that further human activities, river regulation and large-scale changes in biomorphic processes have led to a significant reduction in the channel width, activity area and channel activity of the Ebro River, and made recommendations for the protection and restoration of the river ecosystem. The calculation of channel activity generally requires the use of the channel centerline. Boothroyd et al. [28] share a demonstration workflow to extract active river channel masks from a section of the Cagayan River (Luzon, Philippines) and then quantify centerline migration rates from multitemporal data, revealing the advantages of the GEE platform for channel migration studies that can use large geospatial data. The polygonal axis generated by the transformation of the channel boundary line was a relatively common and classic method for determining the centerline in the past [29]. However, more and more algorithms for extracting centerlines are emerging. Pavelsky and Smith [30] proposed RivWidth, which derives the channel centerline via raster-based inundation classification, and the uncertainty of accuracy depends mainly on the quality of water classification. Yang et al. [31] developed RivWidthCloud on the GEE platform based on RivWidth, which allows users to easily use the huge amount of remote sensing data available on the platform to calculate the centerline of the channel in the image. These two algorithms for extracting the channel centerline are both based on water index calculations. With the development of remote sensing technology, more and more new water indexes have emerged. Different water indexes can achieve good extraction results for different underlying surfaces. For example, the normalized difference water index (NDWI) is suitable for underlying surfaces with soil and vegetation [32], and the modified normalized difference water index (MNDWI) has a better water extraction effect in urban areas [33], while the automated water extraction index (AWEI) can remove urban and mountain shadows, and is used when there are many shadows [34]. The use of various water indexes broadens the applicability of RivWidthCloud and greatly expands the range of applications of water indexes on river channels.

Although there are more studies on river channel migrations, most of them focus on the development and changes of bends on the channel [1,2,15,26], and there are fewer studies on the changes of the channel on a large scale. In addition, there are still several deficiencies in previous studies on river channel migrations. First, due to data reasons, old maps and documents are frequently used in the study of channel migrations, and their

accuracy needs to be considered. Secondly, the delineation of the boundary and centerline of the river channel in a large area is somewhat subjective, and the migration rate of the channel needs to be evaluated objectively. Finally, due to the low degree of automation, it is cumbersome to repeatedly measure the change of the river channel over time, requiring a lot of manpower. Therefore, previous studies on river channel migration faced problems of data, accuracy, subjectivity and automation that could not be satisfied at the same time (e.g., the use of aerial photography by drones introduces problems of small regional and temporal scales, and the use of old maps introduces problems of low accuracy). Based on the deficiencies of previous studies, a new algorithm or model is urgently needed for the study of river channel migrations to complete the detection of large-scale and long-term time series required for channel changes. Moreover, the algorithm or model must satisfy objectivity and a certain degree of accuracy, to reduce the large investment of manpower and material resources required to monitor the change of the river channel.

In order to obtain large-scale regional and long time series information on river channel migrations, CARSM was established in this paper with the Lower Yellow River (Zhengzhou-Jinan section) in China as the study area. We also analyzed the changes of channel activity in the Lower Yellow River before and after the completion of Xiaolangdi Reservoir. Specifically, this paper attempts to achieve two objectives: (1) to develop a remote sensing model that can effectively represent large scale and long time series channel migrations; (2) to segment the channel in the study area, calculating and analyzing the overall and segmented channel activity changes in the Lower Yellow River and delineating the risk zones.

2. Study Area and Data

2.1. Study Area

The Yellow River originates in the Bayan Har Mountains and flows into the Bohai Sea, which is the second-largest river in China. The section of the Yellow River below Taohuayu in Zhengzhou, Henan Province, is the lower reaches of the Yellow River, and the middle and lower reaches are segmented based on geomorphological topography and hydrological characteristics. The middle reaches of the Yellow River have deep valleys, narrow curved channels and swift currents, which carry a large amount of sediment through the Loess Plateau. The lower reaches of the Yellow River are wide and shallow, with a scattered water flow. Due to the middle reaches of the Yellow River resulting in siltation and high riverbeds, it is difficult for surrounding rivers to converge. The lower reaches of the Yellow River are 786 km long, with a drainage area of 23,000 km². The total drop of the lower reaches is 93.6 m, with an average specific drop of 0.012%. The current river bed is 4–6 m above the ground level of the back river, and it is a world-famous “hanging river on the ground”. River sediment erosion and sedimentation change dramatically, with the river wandering and being changeable. The floods are gathered in the upper and lower reaches; the lower reaches of the Yellow River are an important section of flood control. In addition to the low hills between Dongping Lake and Jinan on the south bank of the river, the rest of the river is held back by dikes, with a total length of more than 1400 km.

In order to study the changes in the channel migration rate due to siltation sediment in the Lower Yellow River, the Zhengzhou-Jinan section (113.56–116.84°E, 34.72–36.33°N) in the Lower Yellow River is taken as the study section in this paper (Figure 1). There are no relevant tributaries in the study areas and the river system is dominated by the main stem only. Its length is more than 300 km. Due to the siltation in the main channel of the Lower Yellow River, the channel stability is poor and because the channel is wide and shallow, this has led to frequent channel migration in the study section. In order to stabilize the main channel, numerous channel improvement works were carried out, including embankment works and the construction of reservoirs. In the 1990s, the Xiaolangdi Reservoir was built on the braided section of the river and at the exit of the last canyon in the middle reaches of the Yellow River, and the Xiaolangdi Reservoir was also put into use in the autumn of 1999. The purpose was to regulate the sediment entering the Lower Yellow River, artificially

change the relationship between water and sediment in the Lower Yellow River, prevent and control floods, and stabilize the river channel in the Lower Yellow River.

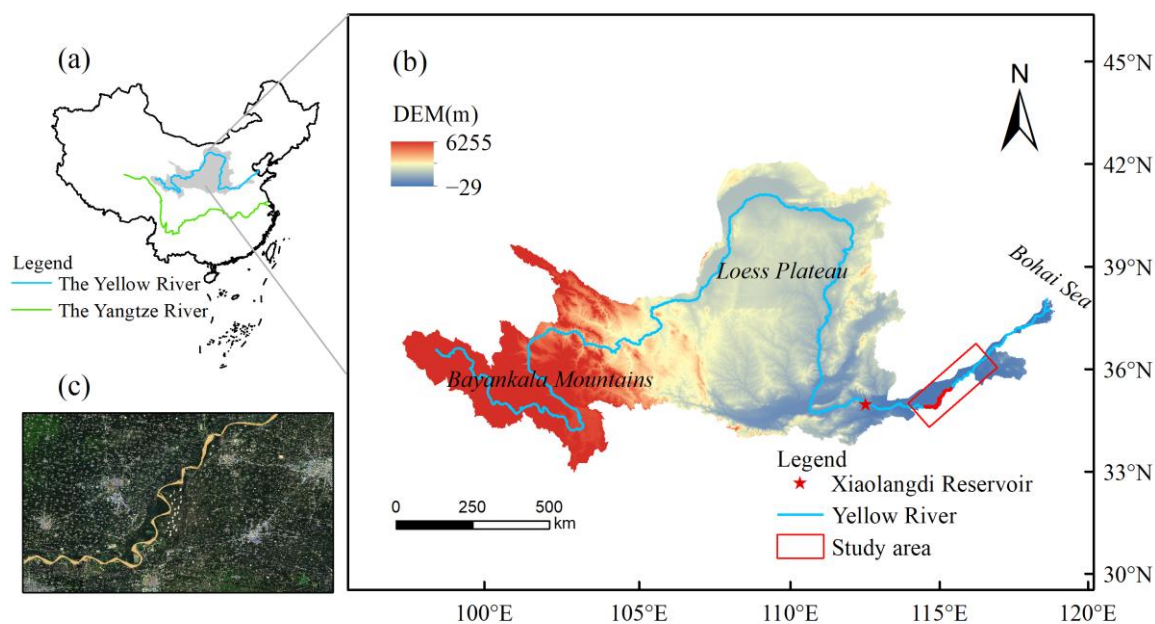


Figure 1. Overview of the study area. (a) The Yellow River basin (shaded area) and the Yellow River (blue line) in China; (b) DEM of the Yellow River Basin and location of the studied river section (inside the red box)—the DEM data are derived from the SRTM V3 product available for download on the GEE platform (https://developers.google.com/earth-engine/datasets/catalog/USGS_SRTMGL1_003, accessed on 9 July 2023); (c) true color plan of the studied rivers (their locations are marked in red in (b)).

2.2. Data

The GEE platform is a cloud computing platform specialized in processing satellite images and other earth observation data. The platform stores a large amount of remote sensing data, and users are free to create new algorithms or reorganize them to process remote sensing data according to their research needs, without the constraints of inherent algorithms. The Landsat series satellites were developed and launched in cooperation between NASA and the US Geological Survey. So far, Landsat has launched a total of nine satellites. The Landsat series of image data includes all land areas from a latitude of 83° north to 83° south, with image updates every 16 days. Landsat series satellites can monitor the rational use of agriculture, forestry, animal husbandry and water conservancy resources by taking images of various targets.

The images of Landsat have a spatial resolution of 30 m and the channel could be clearly identified. Landsat has been launched for a long time and many historical images are available, so it is used as research data to analyze channel activity and changes in the Lower Yellow River. All Landsat raw data values are converted into surface reflectance values using a multiplicative constant (0.0000275) and additive constant (−0.2) on the GEE platform. A total of two Landsat scenarios were covered in the study area using Landsat Thematic Mapper (TM) and Operational Land Imager (OLI) level2 data products on the GEE platform. In order to obtain the maximum visibility of the channel, remote sensing images with cloud cover of less than 20% were used; combined with the regional geographical environment and the history of water conservancy construction in the upper reaches, a total of four views of Landsat images were selected for the study channel section between 1990 and 2020 (Table 1). The data were obtained in September when the water level was high after the flood season. The basis for selection is that the rainfall after the flood season is less and stable, and the morphology of the channel can be clearly identified through the images, which is convenient for comparing changes in channel activity. The

longest time span of the selected image is 30 years, and the time span between two adjacent images is about 10 years, so that the selected time span images can fully reflect the channel activity and its changes. In 1990, 2000 and 2009, images from Landsat-5 TM sensors were used, and in 2020, images from Landsat-8 OLI sensors were used.

Table 1. The dates of Landsat image used and the situation of sand regulation and water regulation of the Xiaolangdi Reservoir.

| Date | Sensor Type | Resolution (m) | Major Events of Xiaolangdi Reservoir before Date |
|-------------------|-------------|----------------|---|
| 2 September 1990 | TM | 30 | The Xiaolangdi Reservoir had not been built |
| 13 September 2000 | TM | 30 | The Xiaolangdi Reservoir in operation |
| 22 September 2009 | TM | 30 | A total of 9 rounds of sand and water regulation in the Xiaolangdi Reservoir |
| 4 September 2020 | OLI | 30 | A total of 10 rounds of sand and water regulation in the Xiaolangdi Reservoir |

Water and sediment data from 1950 to 2020 at the Huayuankou hydrological station, which were obtained from the National Earth System Science Data Center (<http://geodata.cn/>), were used in this paper to analyze the changes in water and sediment in the lower Yellow River before and after the completion of Xiaolangdi Reservoir.

3. Methods

The flowchart of CARSM in this paper is shown in Figure 2, which contains a total of three modules. The first module obtains water boundaries from remote sensing images; the second module extracts channel centerlines from water boundaries; the third module calculates channel activity based on overall and segmental channel centerlines.

3.1. Extraction of Channel Boundary

In this study, the method of the water index combined with the threshold value is used to extract channel information from the selected remote sensing images. The underlying surface of the Lower Yellow River is mainly composed of water bodies, bare land, vegetation and buildings. The characteristics of the reflection spectrum of the water are as follows: high reflection in the blue and green band, and low reflection in other bands, especially near-infrared and mid-infrared bands, which are close to 0. This is the main difference between the water and other ground objects in the spectrum. Therefore, many water indexes enhance water information and suppress non-water information based on the relationship between bands [32–36]. The normalized difference water index (NDWI) is the first proposed water index. The NDWI is calculated using green and near-infrared bands [32], which suppresses the effect of vegetation and bare ground on water extraction. The MNDWI proposed by Xu [33] replaces the original near-infrared band with the mid-infrared band, which solves the problem of NDWI easily extracting buildings as water. The equation is as follows:

$$\text{MNDWI} = (\text{Green} - \text{Swir}) / (\text{Green} + \text{Swir}) \quad (1)$$

where Green and Swir represent the green band and mid-infrared band of Landsat image level-2 products, respectively.

Then, since the values of the MNDWI images after enhancing the water information are between -1 and 1 , without much noise interference, and the MNDWI value of water is quite different from the MNDWI value of other objects, they are suitable for image segmentation algorithms that are divided into two categories. Hence, an automatic threshold selection

method (Otsu) is used to determine the threshold values of the MNDWI images. The principle of Otsu [37–39] is to traverse all thresholds, then divide the image into target and background according to the traversed thresholds, calculate the inter-class variance values between the pixels of all thresholds, and take the threshold corresponding to the largest inter-class variance value as the optimal threshold. The equation of Otsu is as follows:

$$\sigma^2 = \sigma_W \sigma_N (\mu_W - \mu_N)^2 \quad (2)$$

$$T = \max(\sigma^2) \quad (3)$$

where σ_W and μ_W represent the proportion of the target (water) to the total image and the average pixel value, and σ_N and μ_N represent the proportion of background (non-water) to the total image and the average pixel value of the image. The optimal threshold, T , for segmenting the image is obtained when the traversal threshold segments the image to obtain the maximum interclass variance.

Using the MNDWI combined with the optimal threshold calculated by Otsu [37], the water in the Lower Yellow River can be well-separated from the background, to obtain the water mask image.

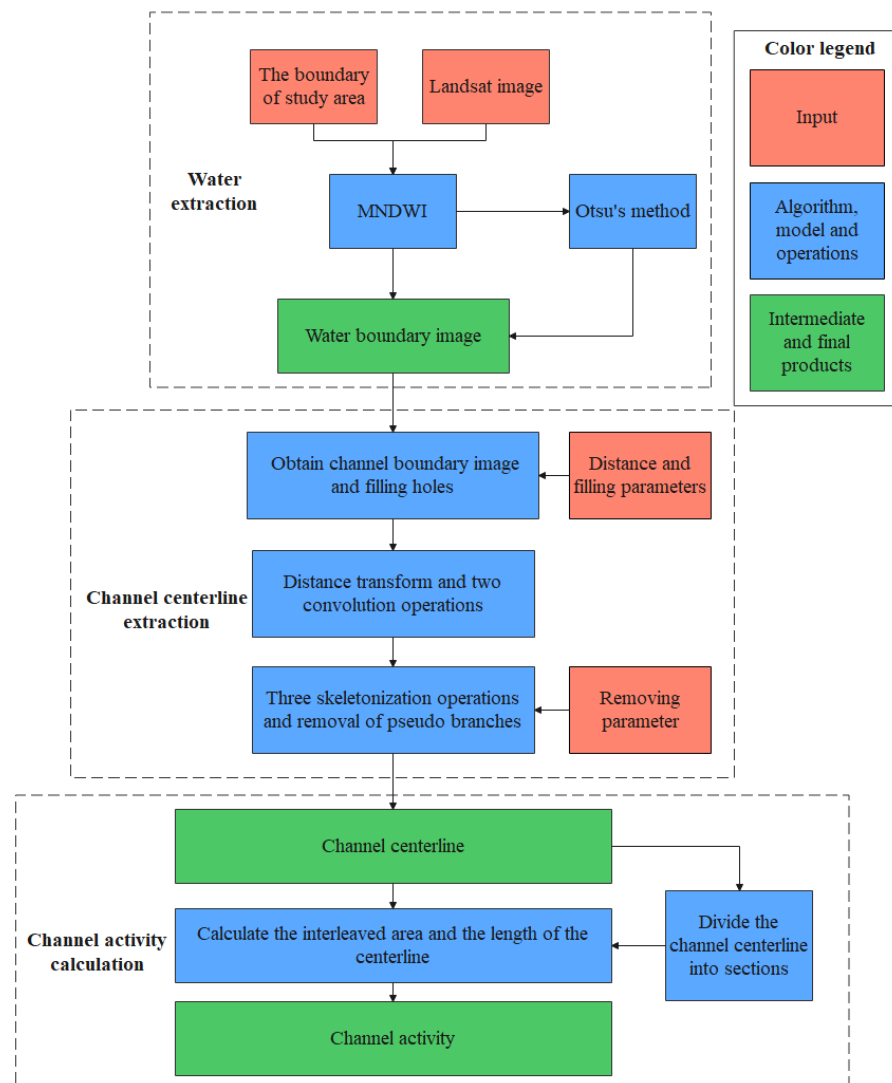


Figure 2. The flowchart of CARSM. The red box represents the input part, the blue box represents the algorithm, model or operation part, and the green box represents the final product or intermediate product part.

3.2. Extraction and Subsection of Channel Centerline

In this paper, RivWidthCloud is used to extract the channel centerline from the water mask image. RivWidthCloud is an automatic Google Earth Engine algorithm for extracting channel centerlines and channel widths from remote sensing imagery [31]. The original RivWidthCloud extracts the centerline of the channel from remote sensing images in seven steps:

Step 1: The method proposed by Zou et al. [40] is used to extract water on a Landsat image. The principle of this water extraction procedure is based on the spectral water classification in Equations (4)–(6). The water mask image is obtained via the joint extraction of the MNDWI, normalized difference vegetation index (NDVI), and enhanced vegetation index (EVI) [33,41,42].

$$\text{NDVI} = (\text{Nir} - \text{Red}) / (\text{Nir} + \text{Red}) \quad (4)$$

$$\text{EVI} = 2.5 \times (\text{Nir} - \text{Red}) / (1 + \text{Nir} + 6 \times \text{Red} - 7.5 \times \text{Blue}) \quad (5)$$

$$\text{water} = ((\text{MNDWI} > \text{NDVI}) \text{ or } (\text{MNDWI} < \text{EVI})) \text{ and } (\text{EVI} < 0.1) \quad (6)$$

where Nir, Red, and Blue represent the near infrared band, red band and blue band of Landsat image level-2 products, respectively.

Step 2: Channel pixels and non-channel water pixels based on the global river width of the Landsat (GRWL) dataset are distinguished from each other. The water beyond 4 km (this is an optional distance) from the GRWL centerline is removed to obtain the channel boundary.

Step 3: Foreign objects (islands and dams) with a fill area of less than 0.3 km² (this is the optional size) are filled and the filled image is called the channel mask image.

Step 4: A distance transform operation is performed on the channel mask image, and the distance transform operation assigns a channel pixel to the nearest non-channel pixel. After the distance transform operation, pixels near the center of the channel have a local maximum.

Step 5: The distance-transformed image is convolved with a pair of 3 × 3 pixel kernels (7–8) to generate a gradient image, The gradient of pixels close to the centerline is almost always a local minimum and close to 0. A threshold of 0.9 is usually used to generate the initial centerline.

$$\begin{bmatrix} \frac{1}{8} & 0 & -\frac{1}{8} \\ \frac{3}{8} & 0 & -\frac{3}{8} \\ \frac{5}{8} & 0 & -\frac{5}{8} \\ \frac{7}{8} & 0 & -\frac{7}{8} \end{bmatrix} \quad (7)$$

$$\begin{bmatrix} -\frac{1}{8} & -\frac{2}{8} & -\frac{1}{8} \\ 0 & 0 & 0 \\ \frac{1}{8} & \frac{2}{8} & \frac{1}{8} \end{bmatrix} \quad (8)$$

Step 6: A skeletonization operation is applied three times to the initial centerline to produce a centerline that is only one pixel wide [43].

Step 7: These branches are trimmed by starting from the endpoint of each centerline and removing either 500 pixels (this is an optional length) or the total length of the segment to the next confluence, producing the channel centerline with no pseudo-branches that is only one pixel wide.

The original RivWidthCloud requires the ID of a single Landsat image as input to generate the river centerline for a single image, as water extraction via the original algorithm is not effective at the boundary of the channel in this study area, and the center of the channel is also easy to miss in extraction. In order to enable the algorithm to be available on a large scale and to match the characteristics of the Lower Yellow River substrate, a more suitable water extraction method needs to be used. In this paper, the algorithm is

improved by first stitching the Landsat image and then using the mask map obtained via MNDWI combined with Otsu's method on the image instead of using the water mask map method of Zou et al. to obtain the water mask image as input. Additionally, the parameters of distance, filling and removal are selected according to the geography of the Lower Yellow River to extract the centerline of the channel. The source code for extracting channel centerline in CARSM can be accessed directly in GEE at https://code.earthengine.google.com/?accept_repo=users/zenan990218/CARSMPaper (accessed on 9 July 2023).

Meanwhile, in order to explore the change in channel activity between the overall and local channels in the Lower Yellow River, all the obtained centerlines were divided into 30 segments. The specific method of segmentation is to divide the channel centerline of the latest year (2020) into 30 equal parts, and then generate a normal perpendicular to the centerline of the channel at each endpoint of the divided centerline, and finally extend the normal to intersect the centerlines of the other years to obtain the intersection, which is the endpoint of the 30 segments of the other years.

3.3. Channel Activity Remote Sensing Retrieval Model

Channel activity is the average rate of lateral migration along a channel per unit time and can be measured in a variety of ways. According to the characteristics of slight change in local width and the low complexity of the channel graph in the Lower Yellow River, this paper uses the channel centerline to calculate the channel's activity. The specific method to calculate the channel activity is to use the geometric relationship between the channel centerlines in different years, and use the integral form to obtain the length of the channel centerline in the earlier year and the sum of the area of the polygon surrounded by the two channel centerlines. Finally, the sum of the areas is divided by the time span between the centerlines of the two channels and then divided by the length of the centerlines in the previous year, so that the channel activity under the time span can be obtained. Since the four Landsat images have a certain lateral offset in the spatial range of the study area, all images include the end of the downstream channel in the study area. However, the starting points of the channels in the four images are not consistent, so when calculating the channel's activity, it is necessary to take the common intersection area of the four images, to ensure that the channel's activity in the same area is calculated. In Figure 3 is a schematic diagram illustrated for calculating channel activity in this paper, and its calculation equation is as follows:

$$M = S/[T_2 - T_1]/L_1 \quad (9)$$

$$S = \int_a^b |f_1(x) - f_2(x)| dx \quad (10)$$

$$L_1 = \int_L 1 ds \quad (11)$$

where M represents the channel's activity and S represents the sum of the areas of the geometric figures enclosed by the intertwined centerlines in different years. L_1 represents the centerline length of the earlier of the two centerlines, and T_1 and T_2 represent the image date of the earlier year and the image date of the latter year, respectively. $f_1(x)$ and $f_2(x)$ represent the centerline curve trajectories of the channel in earlier and later years, respectively. a and b represent the horizontal coordinates of the starting point and end point of the curve, respectively. dx represents the differential along the horizontal coordinate. L represents the integral route along the channel in the earlier year and ds represents the differential along the channel in the earlier year.

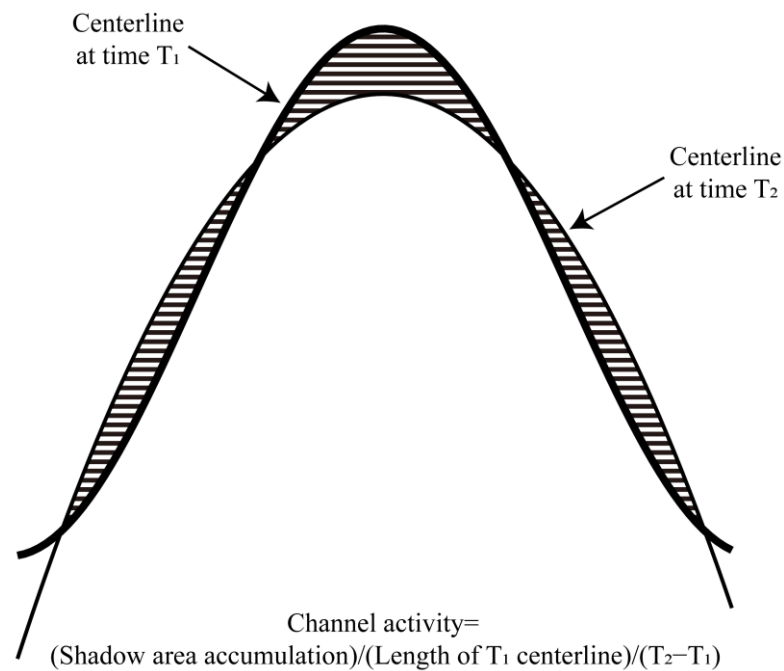


Figure 3. Procedure for calculating channel activity from the channel centerline. The dark black line represents the channel centerline of the previous time and the light black line represents the channel centerline of the next time.

4. Results

4.1. Model Parameters and Thresholds

CARSM needs to set the water extraction method and the parameters that need to be paid attention to when extracting the centerline. Based on factors such as water and bare land vegetation occupying the main underlying surface near the Lower Yellow River, the MNDWI combined with Otsu's method was selected as the water extraction method in this paper. In extracting the centerline, due to the large width of the Lower Yellow River and the relatively small number of small islands in the center of the river, a foreign object filling less than 333 image elements (i.e., 0.3 km²) was set to reduce the complexity of digitization and avoid unnecessary segmentation, set to remove water beyond the maximum distance of 6000 m from the channel bank to the channel centerline and set to trim pseudo-branches of less than 100 pixels (i.e., 3000 m).

The MNDWI images calculated from four images of different years are shown in Figure 4. The value of the MNDWI of water in the channel is larger than that of other surface features and the proportion of the channel in the entire image is small, and only exists in a small part of the image center.

The histograms of the MNDWI images calculated from four images of different years and the interclass variance between two features calculated according to different thresholds are shown in Figure 5. From the four histograms, we can know that because the river channel is wider and occupies a smaller proportion in the image, we can assume that the histogram of the image has a double peak and there is a large gap between the double peaks, but the double peak phenomenon is not particularly significant. From the four interclass variance images, we can know that the interclass variance between the two features increases and then decreases as the threshold value increases from -1 to 1. The threshold value at the maximum interclass variance is basically in the range of 0 to 0.1. The optimal threshold values at the maximum interclass variance calculated by Otsu for these four MNDWI images are shown in Table 2.

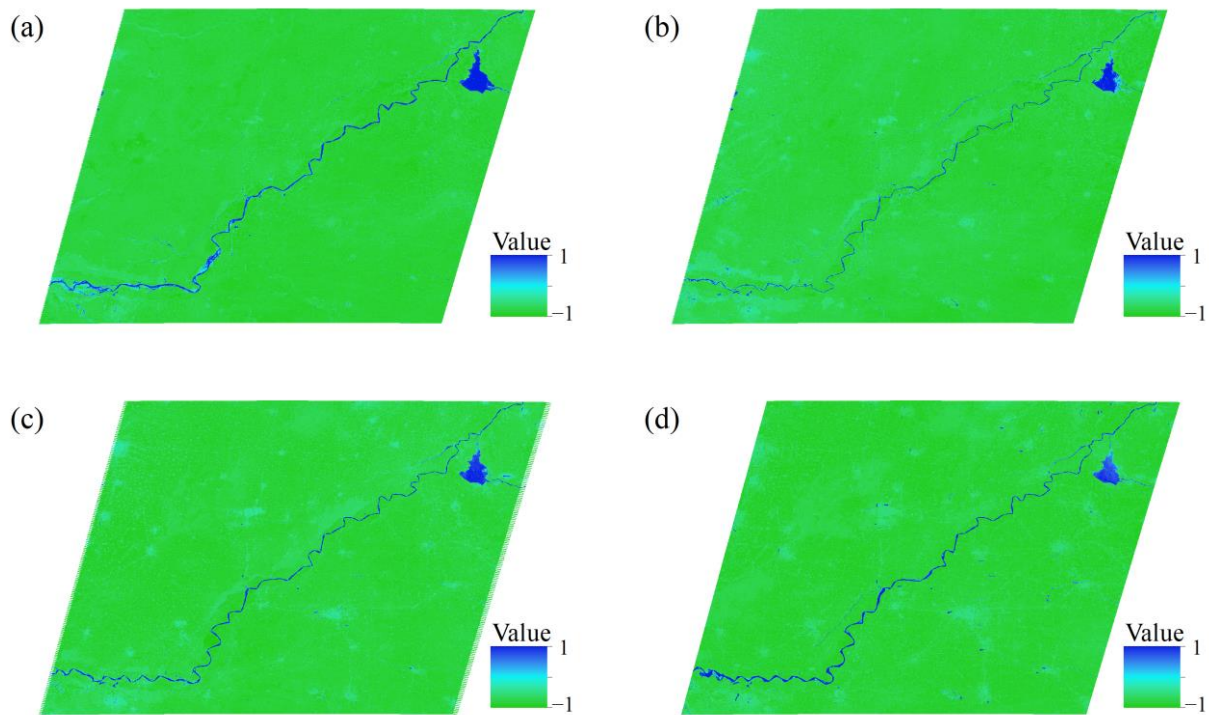


Figure 4. The MNDWI images calculated from the MNDWI. (a) MNDWI image in 1990; (b) MNDWI image in 2000; (c) MNDWI image in 2009; (d) MNDWI image in 2020.

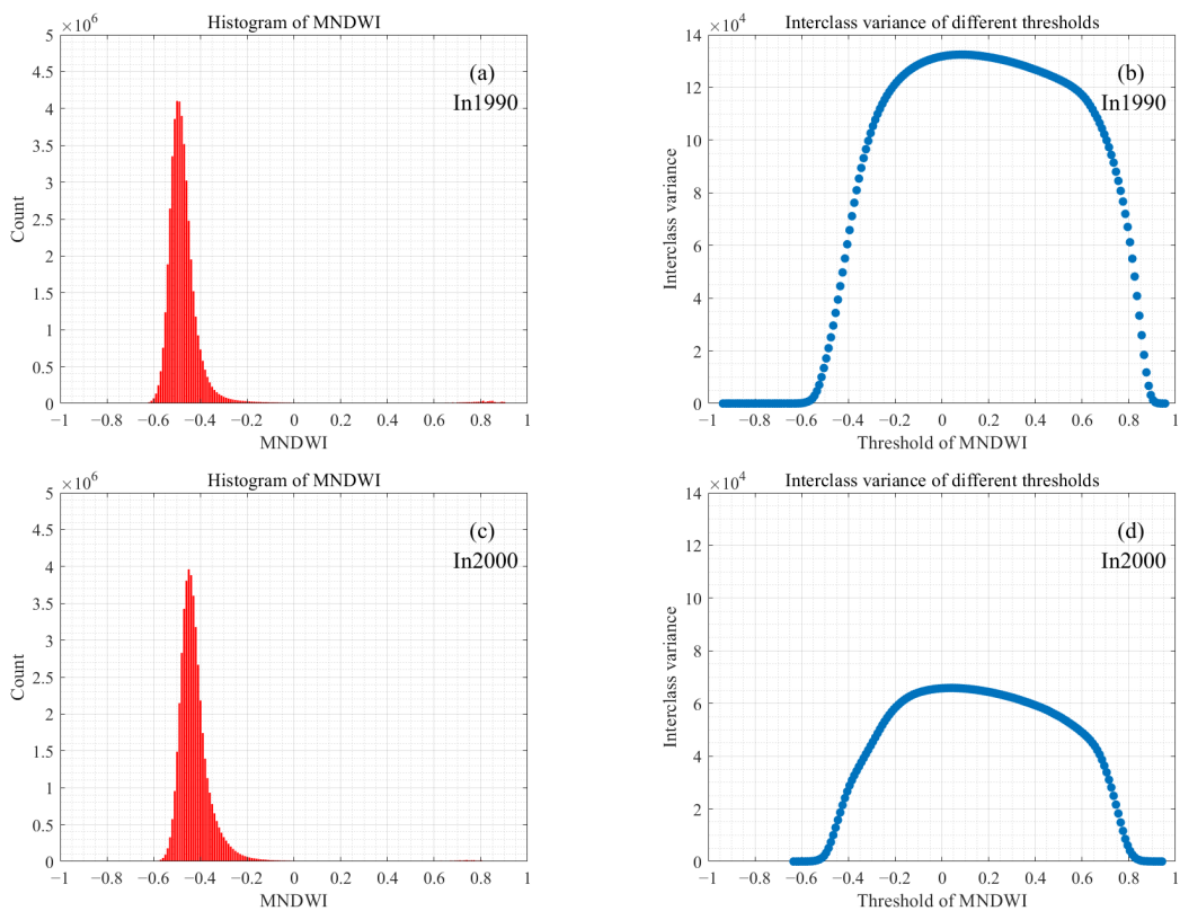


Figure 5. Cont.

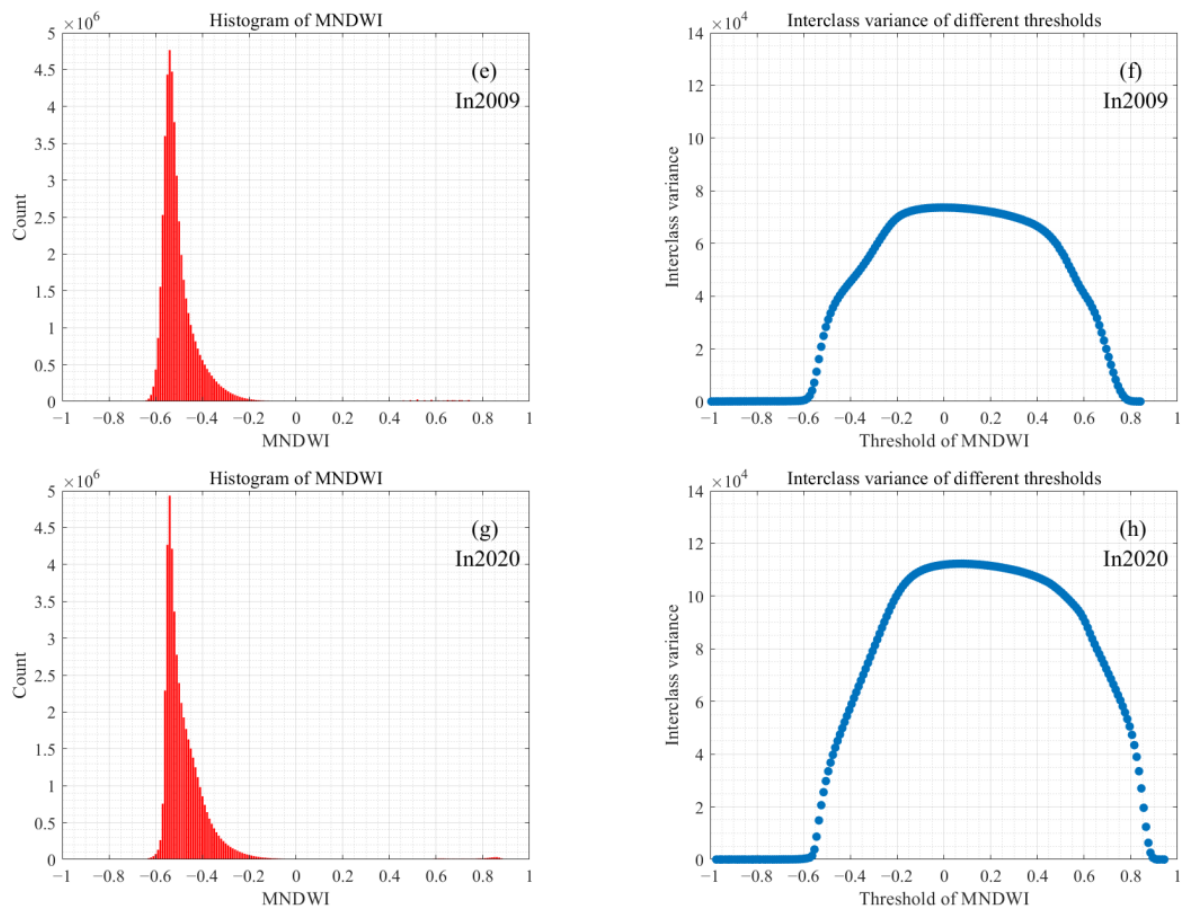


Figure 5. The histograms of MNDWI images and interclass variance for different thresholds. (a) MNDWI histogram in 1990; (b) interclass variance in 1990; (c) MNDWI histogram in 2000; (d) Interclass variance in 2000; (e) MNDWI histogram in 2009; (f) interclass variance in 2009; (g) MNDWI histogram in 2020; (h) interclass variance in 2020.

Table 2. The optimal threshold value obtained according to the maximum variance between classes.

| Year | Optimal Threshold |
|------|-------------------|
| 1990 | 0.0850 |
| 2000 | 0.0351 |
| 2009 | −0.0050 |
| 2020 | 0.0750 |

The channel boundary images extracted after the water image is extracted according to the optimal threshold combined with the MNDWI image and then according to the centerline parameter setting are shown in Figure 6. From Figure 6, we can know that the general position of the Lower Yellow River remains stable during the four time periods, the flow direction of the river is first to the east and then to the northeast, and there is a Dongping Lake reservoir in the northeast of the study area. This characteristic of the one-way channel in the study area is obvious, that is, there is basically only one main road and basically no other tributary flows into it.

The contents of the four channel centerlines extracted via RivWidthCloud according to the channel boundaries in different years are shown in Table 3. including the length, S , of the centerline of these rivers according to the centerline of the rivers, respectively, and the distance, l , of the geometric plane between the beginning and the end of the rivers. The curvature of the four rivers is calculated according to the equation of the definition of the curvature of the rivers $K = S/l$. It can be seen from the table that the curvature of the Lower

Yellow River increases sharply before the construction of Xiaolangdi Reservoir, and then decreases slowly after the reservoir is put into use.

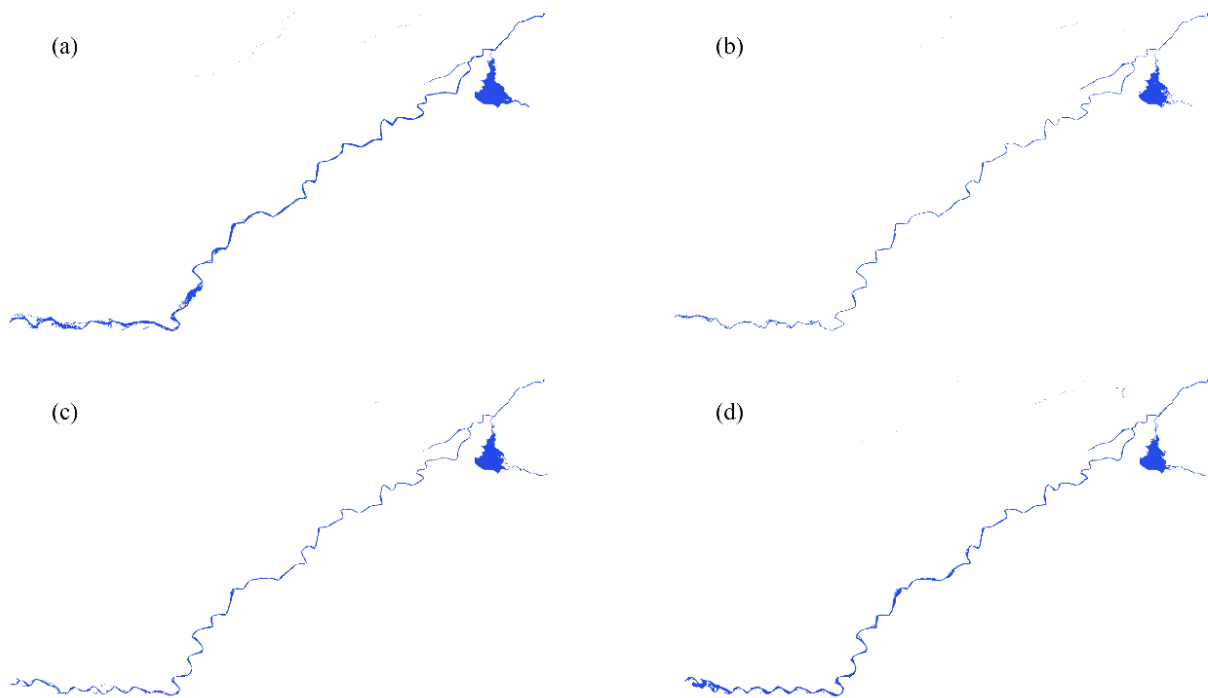


Figure 6. The images of channel boundaries in different years. (a) The channel boundary in 1990; (b) the channel boundary in 2000; (c) the channel boundary in 2009; (d) the channel boundary in 2020.

Table 3. Specific information on the channel centerlines.

| Year | Centerline Length (km) | Straight Channel Length (km) | Curvature |
|------|------------------------|------------------------------|-----------|
| 1990 | 363.38 | 265.30 | 1.370 |
| 2000 | 384.02 | 264.41 | 1.452 |
| 2009 | 379.85 | 264.33 | 1.437 |
| 2020 | 375.73 | 264.28 | 1.422 |

The planar conditions of the channel centerline in four different years are shown in Figure 7, and these four centerlines are morphologically intertwined, indicating repeated channel changes in the Lower Yellow River. It can also be seen that the first half of the four intertwined centerlines are intertwined and intersect more, while the second half of the centerlines are closely spaced and intersect less. This shows that the position of the first half of the Lower Yellow River changes dramatically and frequently, and the position of the first half of the channel changes significantly; the second half of the channel is less intertwined and relatively stable, and the position of the second half of the channel does not change significantly.

4.2. The Result of CARSM

The channel activity of the Lower Yellow River for three time periods, 1990–2000, 2000–2009, and 2009–2020, are shown in Figure 8, where the overall and segmented channel activity are calculated separately for each time period to explore the changes in channel activity of the Lower Yellow River.

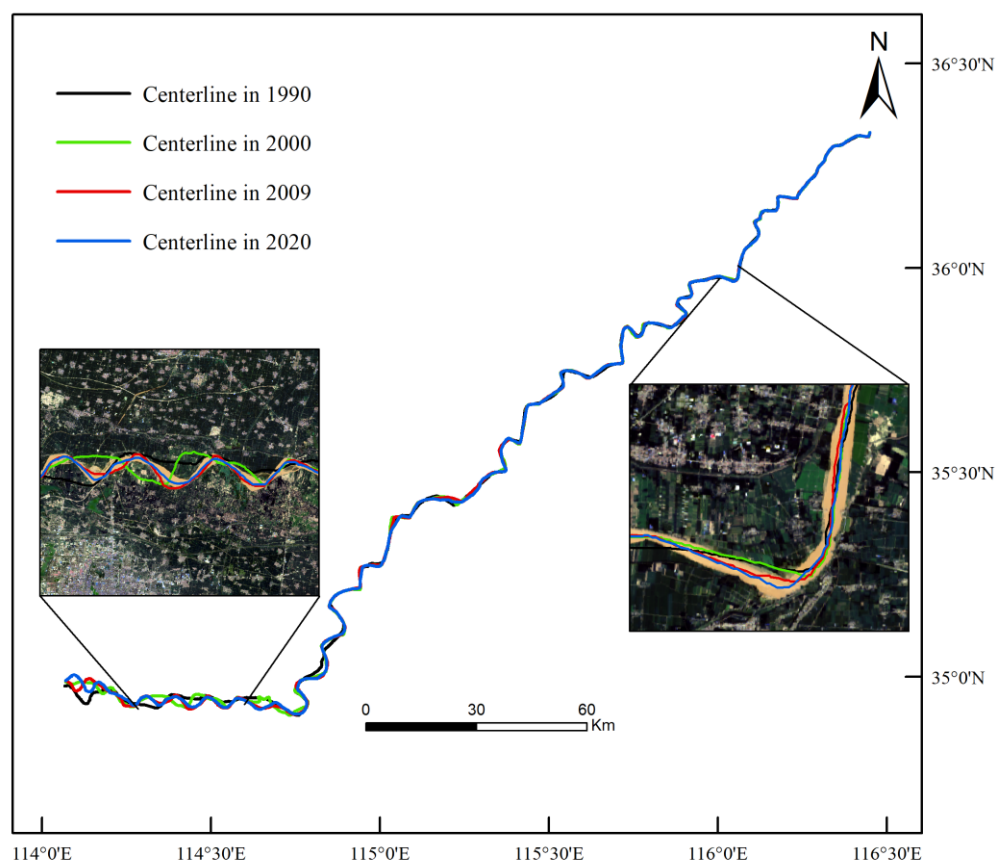


Figure 7. The extraction result of the channel centerline. The black line in the figure indicates the channel centerline in 1990, the green line indicates the channel centerline in 2000, the red line indicates the channel centerline in 2009, and the black line indicates the channel centerline in 2020. The background of the enlarged images are the true color image of 2020.

From a general perspective, the overall channel activity between 1990 and 2000 was 41.35 m/year; it was 27.69 m/year for 2000–2009 and 16.32 m/year for 2009–2020, and their migration rates are highly dependent on the year. Although the overall channel activity was generally higher in the three time periods, the overall channel activity in the three time periods decreased gradually. The reduced values are 13.66 m/year and 11.37 m/year, respectively, and the proportions of decline were 33.04% and 41.06%, respectively, which indicated that the activity of the Lower Yellow River decreased and the overall migration rate of the Lower Yellow River channel slowed down.

From a segmental perspective, the channel activity in the upstream part of the study reach (before segment 10) was generally higher than the overall channel activity, and the channel activity in the downstream part of the study reach (after segment 10) was generally lower than the overall channel activity. This indicates that the upper reaches of the channel are unstable, with high variability in channel location and high activity, while the lower reaches of the channel are more stable, with little variability in channel location and low activity. The segmented channel activity for the three time periods also follows the same trend as the overall channel activity does (gradually decreasing). However, in the middle and lower reaches, there are individual segments where the channel activity exceeds the overall channel activity. For example, the channel activity of segment 15 from 2000 to 2009 and 2009–2020 is both higher than the overall channel activity in this time period, indicating that this segment is more active.

The stability of the channel after segmentation is judged by whether or not the segmental activity is less than ten percent of the overall activity, and it can be analyzed from Figure 8 that the channel in the upper half of the study area is gradually becoming stable.

The segmented channel activity was ten percent lower than the overall channel activity for the first time in segment 10 during 1990–2000, compared to that of segment 9 obtained for the first time during 2000–2009, and segment 5 obtained for the first time during 1990–2000. The segmentation of the river with lower post-segmentation channel activity than the overall channel activity is gradually moving forward, and it can be analyzed that the upstream of the study area is changing from turbulent to stable, and slowly becoming stable from the downstream direction to the upstream direction.

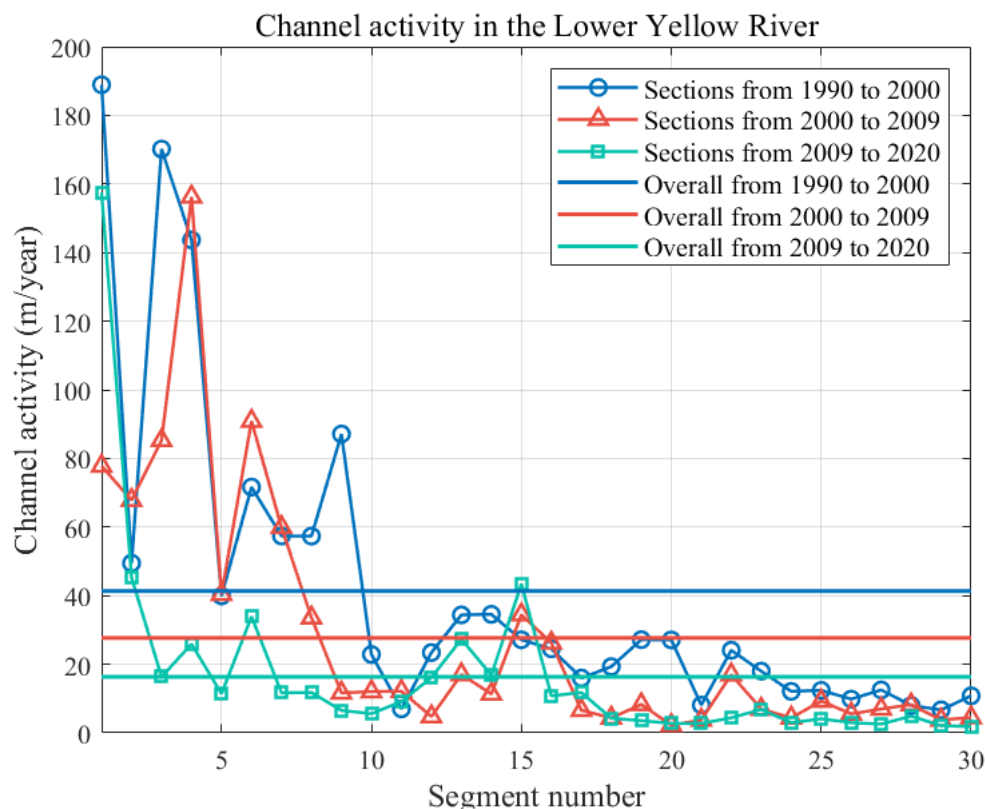


Figure 8. The changes in overall and segmental channel activity in the Lower Yellow River. Lines of the same color are used in the same time period, and the lines with marks represent the segmental channel activity, while the lines without symbols represent the overall channel activity.

4.3. Channel Risk Demarcation

The area after each segment was classified as a risk zone based on the number of time periods in which the segmented channel activity was lower than the overall channel activity. The segments with higher channel activity than the overall channel activity in all three time periods were classified as high-risk zones; the segments with higher channel activity than the overall channel activity in two time periods were classified as medium-risk zones; and the segments with higher channel activity than the overall channel activity in one time period were classified as low-risk zones. If the channel activity of a segment is lower than the overall activity in the all three time periods, it is classified as a safe zone. The risk zones to which the segmented rivers belong are shown in Table 4, of which there are 5 high-risk zones, 4 medium-risk zones, 2 low-risk zones and 19 safety zones.

Table 4. The result of risk zone classification.

| Risk Classification | Segment Number |
|---------------------|----------------|
| High-risk zones | 1–4, 6 |
| Medium-risk zones | 5, 7, 8, 15 |
| Low-risk zones | 9, 14 |
| Safety zones | 10–13, 16–30 |

5. Discussion

5.1. Characteristics of CARSM

Using channel activity to simplify the complex channel movement model into a model with only the initial state and the end state and quantitatively calculating the average value of the overall lateral migration of the channel provides a means to study the normal state of the channel and its changing characteristics. In this paper, a remote sensing inversion model for channel activity is proposed for the first time, and due to the high portability of the model, it can not only use Landsat imagery but also be extended to include other remote sensing data products (such as Sentinel-2, MODIS or other microwave satellite images) relatively easily. Satellite images with different characteristics may play different roles in later studies of channel migration. In addition, the model has several characteristics of its own, and the following are some characteristics of CARSM.

CARSM can combine both temporal and spatial resolution. Since there are many channels on the surface and considering the fact that channel migration is a long and slow process, monitoring and research on channels often require a long time series and sufficient amount of data. In previous studies, field measurements, historical maps, aerial photographs or other historical documents were often selected as reference data for research; however, previous methods suffer from less available data, low precision and relative difficulty in calculation, and their temporal and spatial resolution needs are often not met simultaneously. With the proliferation of various satellite images, a series of large satellite missions such as Landsat have the advantages of global coverage, routine data collection, high temporal resolution, and a large time span of available images, and more and more images with high temporal and spatial resolution are available for channel activity calculations, meeting both temporal and spatial needs. Using CARSM to calculate channel activity, it is only necessary to stitch images of the same period or similar periods into one image to calculate channel activity, and the remote sensing images stitched with multiple periods can be used to calculate channel activity and its change trend, which expands the scope of using it to calculate channel activity.

CARSM has objective extraction results with uniform standards and equally sized errors. The CARSM in this paper all use the same water index to extract water, and the error comes from two points; the first error comes from the registration error E_1 of the original satellite image, which can be viewed in the metadata of the satellite images. Most Landsat image alignments have a root mean square error of 10 m or less [2], and this error accounts for less than 3% of the average water width of the studied river reach. The second error comes from error E_2 of channel extraction, where the MNDWI reportedly extracted water with an accuracy of more than 96% [34,35]. The equation for calculating the overall error is as follows:

$$E = \sqrt{E_1^2 + E_2^2} \quad (12)$$

According to the previous research on the water index and the calculation of the error formula, the maximum error value, E , will be less than 5%, and the accuracy will be greater than 95%. Compared to manual field measurements and previous studies, the model is objective and has a high degree of confidence with a small relative error.

CARSM calculations are fast and concise. Compared to the calculation methods of channel activity in previous studies, the CARSM proposed in this paper only requires two remote sensing images or synthetic remote sensing images to be selected according to the study date and the type of underlying surface, as well as the use of the water index to calculate the channel activity quickly and accurately. CARSM does not require complex training models, and eliminates the inconvenience of manual field surveys and the use of actual measurement data to assist with calculations, so it is more effective for monitoring channel activity changes at large scales and long time series.

5.2. Geomorphic Interpretation of the Results

Changes in the channel activity of a meander are influenced by river flow, sediment transport, channel morphology and floodplain characteristics [8,13,17,24]. Among these four causes, sediment transport conditions are the main reason for changes in channel activity in the Lower Yellow River, because after the Yellow River flows through the areas with the most severe soil erosion on the Loess Plateau, the sediment content in the mainstream of the Yellow River increases dramatically, resulting in sediment accumulation in the Lower Yellow River.

The change in channel activity in the Lower Yellow River is closely related to the construction and use of the Xiaolangdi Reservoir, as its presence has changed the sediment transport conditions in the Lower Yellow River [44–46]. The study river section is located downstream of the Xiaolangdi reservoir, which is located at the end of the middle reaches of the Yellow River and allows a good ability to monitor the sediment flow into the Lower Yellow River. Xiaolangdi Reservoir, which was put into operation in 2000, is the last large reservoir in the middle reaches of the Yellow River that mainly regulates the Yellow River's water and sediment, and has an important influence on the runoff process in the Lower Yellow River. The income sediment coefficient is usually used in studies as an important parameter influencing channel variability. The income sediment coefficient (defined as $\xi = S/Q$; S is the annual average sand content (kg/m^3), and Q is the annual average flow (kg/m^3)) can be used as a discriminatory indicator for the balance of sand transport in the lower reaches of the Yellow River. The threshold of the incoming sediment coefficient is derived from the study experience of the Yellow River sediment over the years, and when the incoming sediment coefficient is $\xi > 0.015$, siltation occurs in the channel; when $0 < \xi < 0.01$, scouring occurs in the channel; when $0.01 < \xi < 0.015$, the channel is roughly balanced between scouring and siltation [47–50]. The incoming sediment coefficients at the Huayuankou hydrological station from 1950 to 2020 are shown in Figure 9.

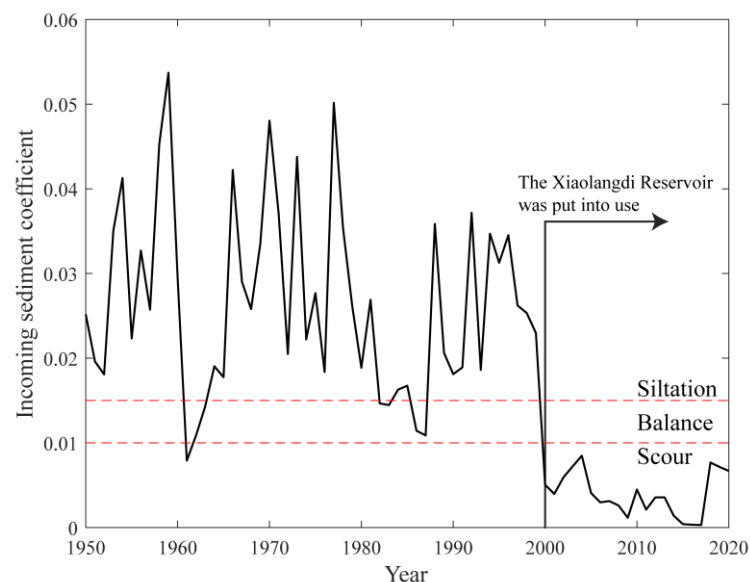


Figure 9. The incoming sediment coefficients at the Huayuankou hydrological station at the end of the Middle Yellow River from 1950 to 2020.

Various measures were carried out on the Loess Plateau for about 20 years from the late 1970s to the late 1990s, but the ecological management of the Loess Plateau did not have a very significant limiting effect on the sediment washed into the Lower Yellow River, while the Xiaolangdi Reservoir came into operation and directly changed the relationship between runoff and sediment in the Lower Yellow River, significantly reducing the amount of sediment transported into the Lower Yellow River while the runoff remained largely unchanged. Before 2000, the value of the incoming sediment coefficient of the Lower Yellow

River was basically between balance and siltation. The slope of the Lower Yellow River was slow, a large amount of sediment was deposited on the bottom of the channel, and the riverbed was constantly rising, which led to the large lateral mobility of the channel. After 2000, the value of the incoming sediment coefficient in the Lower Yellow River was below the critical value of scouring. Some studies have shown that the scour thickness of the main channel in the whole Lower Yellow River after the flood from October 1999 to 2020 was up to several meters, and the scour was more above and less below, with uneven distribution along the course. The reduction in sediment accumulation in the riverbed and the rise in the relative height of the slope banks on both sides of the channel have led to the weakening of the lateral mobility of the channel. This is due to the main role of sand fixation and the drainage of the Xiaolangdi reservoir, which transformed the original siltation-based water sediment pattern of the Lower Yellow River into an impact-based water sediment pattern [51–54], which has led to lower water levels in the Lower Yellow River and higher banks of the channel. The water-sediment pattern regulated by Xiaolangdi Reservoir and the resulting rise in riverbank height lead to a reduction in channel activity in the Lower Yellow River [55], transforming the channel pattern of the Lower Yellow River into a more stable channel pattern.

The Lower Yellow River tends to be stable, but it does not mean that it has no changes at all. Although its activity has weakened, it is still in a normal and healthy state. The lower Yellow River has become less active, which is good for humans because they can make better use of it, but should be wary of low channel activity that could lead to a reduction in species diversity.

5.3. The Potential Applicability of CARSM

CARSM monitors channel activity and its changes mainly by calculating the centerline of the channel. However, due to the morphological characteristics of the channel and the characteristics of remote sensing satellite images, CARSM may not be applicable in some cases. For example, if there are many clouds and fog in the satellite images, this will greatly affect the threshold value of water index extraction, which will lead to the poor extraction of river information and eventually lead to a large error in channel activity calculation. In addition, the common large-channel bifurcation is also an important factor that affects channel activity calculation [56]. According to the centerline algorithm, if there are large unfilled islands in the channel, there will be branching when calculating the centerline of the channel, and then there will be two or more centerlines in the bifurcated section of the channel; at this point, it may be necessary to use a longer line as the centerline calculation.

In future work, there may be an algorithm for removing clouds and fog from satellite images, and the quality of water classification will continue to improve. At the same time, if it is clear which channel centerline is used to calculate channel activity at forked river sections, the applicability and reliability of CARSM will also continue to improve.

6. Conclusions

Using CARSM to identify channel boundaries and channel centerline information, and to invert overall and segmental channel activity based on CARSM can provide a qualitative and quantitative basis for channel migrations. Compared to the use of previous methods of monitoring channel migrations, the use of remote sensing to extract channel information and study changes in channel activity has the characteristics of wide coverage, more comprehensive information, and a low difficulty of acquisition. This paper studies the changes of channel activity in the Lower Yellow River (Zhengzhou-Jinan section) based on multi-period remote sensing images, and the following main conclusions are obtained:

- (1) A remote sensing model (CARSM) for calculating channel activity was constructed. CARSM can quickly calculate channel activity on images with obvious channel features and fewer clouds above the channel by selecting suitable water index and threshold values according to the characteristics of the underlying surface and the time span. We can use two remote sensing images to calculate channel activity, and

we can also use multiple remote sensing images to study the change characteristics of channel activity.

- (2) The channel activity of the Lower Yellow River was calculated in segments, the areas with higher channel activity were determined according to the segmented and overall channel activity, and then the risk areas were identified according to the number of time periods in which the segmented channel activity was higher than the overall channel activity. Precautions were made in advance to avoid property damage.
- (3) Both the overall and the segment of the Lower Yellow River show a trend of gradually decreasing channel activity from upstream to downstream, and the water and sediment pattern of the Lower Yellow River has changed from siltation to scouring. The channel of the Lower Yellow River has become more stable from the downstream to the upstream section, and it is still within the normal range of channel activity. The increasing stability of the channel is mainly related to the water sediment control function of the Xiaolangdi Reservoir. The stabilization of the Lower Yellow River under water sediment conditions will help to resist the disasters brought about by frequent floods.

Author Contributions: Conceptualization, T.W.; methodology, T.W. and Z.X.; software, Z.X. and R.C.; formal analysis, Z.X. and S.W.; investigation, T.W., S.W. and T.L.; data analysis, Z.X. and R.C.; writing—review and editing, T.W. and Z.X.; visualization, Z.X. and T.W.; supervision, S.W. and T.W.; funding acquisition, T.W. and S.W. All authors have read and agreed to the published version of the manuscript.

Funding: This research was funded by the Specially Appointed Professor program of Jiangsu province and National Natural Science Foundation of China, China (grant No. 42141007) and the Inner Mongolia Autonomous Region Science and Technology Achievement Transformation Special Fund Project (No. 2021CG0045).

Data Availability Statement: The data used in this study were obtained from the following platform: the USGS for Landsat data (<https://earthexplorer.usgs.gov/>, accessed on 13 July 2022). Water and sediment data from 1950 to 2020 at the Huayuankou hydrological station were obtained from the National Earth System Science Data Center (<http://ge.geodata.cn/>).

Acknowledgments: We would like to thank the USGS for providing Landsat data (<https://earthexplorer.usgs.gov/>, accessed on 13 July 2021), and the National Earth System Science Data Center for providing water and sand data (<http://ge.geodata.cn/>).

Conflicts of Interest: The authors declare that they have no known competing financial interest or personal relationships that could have appeared to influence the work reported in this paper.

References

1. Brice, J.C. Evolution of Meander Loops. *Geol. Soc. Am. Bull.* **1974**, *85*, 581. [[CrossRef](#)]
2. Guo, X.; Gao, P.; Li, Z. Morphological Characteristics and Changes of Two Meandering Rivers in the Qinghai-Tibet Plateau, China. *Geomorphology* **2021**, *379*, 107626. [[CrossRef](#)]
3. Gutierrez, R.R.; Abad, J.D. On the Analysis of the Medium Term Planform Dynamics of Meandering Rivers. *Water Resour. Res.* **2014**, *50*, 3714–3733. [[CrossRef](#)]
4. Schumm, S.A. Patterns of Alluvial Rivers. *Annu. Rev. Earth Planet. Sci.* **1985**, *13*, 5–27. [[CrossRef](#)]
5. Rosgen, D.L. A Classification of Natural Rivers. *Catena* **1994**, *22*, 169–199. [[CrossRef](#)]
6. Ollero, A. Channel Changes and Floodplain Management in the Meandering Middle Ebro River, Spain. *Geomorphology* **2010**, *117*, 247–260. [[CrossRef](#)]
7. Li, Z.; Yu, G.-A.; Brierley, G.J.; Wang, Z.; Jia, Y. Migration and Cutoff of Meanders in the Hyperarid Environment of the Middle Tarim River, Northwestern China. *Geomorphology* **2017**, *276*, 116–124. [[CrossRef](#)]
8. Nicoll, T.J.; Hickin, E.J. Planform Geometry and Channel Migration of Confined Meandering Rivers on the Canadian Prairies. *Geomorphology* **2010**, *116*, 37–47. [[CrossRef](#)]
9. Gautier, E.; Brunstein, D.; Vauchel, P.; Roulet, M.; Fuertes, O.; Guyot, J.L.; Darozzes, J.; Bourrel, L. Temporal Relations between Meander Deformation, Water Discharge and Sediment Fluxes in the Floodplain of the Rio Beni (Bolivian Amazonia). *Earth Surf. Process. Landf.* **2007**, *32*, 230–248. [[CrossRef](#)]
10. Shields, F.D., Jr.; Simon, A.; Steffen, L.J. Reservoir Effects on Downstream River Channel Migration. *Environ. Conserv.* **2000**, *27*, 54–66. [[CrossRef](#)]

11. Rinaldi, M.; Gurnell, A.M.; Del Tánago, M.G.; Bussetini, M.; Hendriks, D. Classification of River Morphology and Hydrology to Support Management and Restoration. *Aquat. Sci.* **2016**, *78*, 17–33. [[CrossRef](#)]
12. Alber, A.; Piégay, H. Characterizing and Modelling River Channel Migration Rates at a Regional Scale: Case Study of South-East France. *J. Environ. Manag.* **2017**, *202*, 479–493. [[CrossRef](#)] [[PubMed](#)]
13. Casado, A.; Peiry, J.-L.; Campo, A.M. Geomorphic and Vegetation Changes in a Meandering Dryland River Regulated by a Large Dam, Sauce Grande River, Argentina. *Geomorphology* **2016**, *268*, 21–34. [[CrossRef](#)]
14. Hooke, J.M. Magnitude and Distribution of Rates of River Bank Erosion. *Earth Surf. Process.* **1980**, *5*, 143–157. [[CrossRef](#)]
15. Hudson, P.F.; Kesel, R.H. Channel Migration and Meander-Bend Curvature in the Lower Mississippi River Prior to Major Human Modification. *Geomorphology* **2000**, *28*, 531. [[CrossRef](#)]
16. Richard, G.A.; Julien, P.Y.; Baird, D.C. Statistical Analysis of Lateral Migration of the Rio Grande, New Mexico. *Geomorphology* **2005**, *71*, 139–155. [[CrossRef](#)]
17. Xia, J.; Jiang, Q.; Deng, S.; Zhou, M.; Cheng, Y.; Li, Z.; Wang, Z. Morphological Characteristics and Evolution Processes of Sharp Bends in the Lower Yellow River. *Catena* **2022**, *210*, 105936. [[CrossRef](#)]
18. Magdaleno, F.; Fernández-Yuste, J.A. Meander Dynamics in a Changing River Corridor. *Geomorphology* **2011**, *130*, 197–207. [[CrossRef](#)]
19. Dépret, T.; Thommeret, N.; Piégay, H.; Gautier, E. Can Lateral Mobility Be Restored along a Highly Domesticated Low-Energy Gravel-Bed River? *J. Environ. Manag.* **2023**, *325*, 116485. [[CrossRef](#)]
20. Larsen, E.W.; Premier, A.K.; Greco, S.E. Cumulative Effective Stream Power and Bank Erosion on the Sacramento River, California, USA. *J. Am. Water Resour. Assoc.* **2006**, *42*, 1077–1097. [[CrossRef](#)]
21. Richter, B.D.; Richter, H.E. Prescribing Flood Regimes to Sustain Riparian Ecosystems along Meandering Rivers. *Conserv. Biol.* **2000**, *14*, 1467–1478. [[CrossRef](#)]
22. Robison, T.A.; Barry, J. Geomorphic Survey of Eastern Cascade Streams before and after 1995–1996 floods. *For. Ecol. Manag.* **2001**, *143*, 57–64. [[CrossRef](#)]
23. Carson, M.A.; Lapointe, M.F. The Inherent Asymmetry of River Meander Planform. *J. Geol.* **1983**, *91*, 41–55. [[CrossRef](#)]
24. Constantine, J.A.; Dunne, T.; Ahmed, J.; Legleiter, C.; Lazarus, E.D. Sediment Supply as a Driver of River Meandering and Floodplain Evolution in the Amazon Basin. *Nat. Geosci.* **2014**, *7*, 899–903. [[CrossRef](#)]
25. Hooke, J.M. Spatial Variability, Mechanisms and Propagation of Change in an Active Meandering River. *Geomorphology* **2007**, *84*, 277–296. [[CrossRef](#)]
26. Nanson, G.C.; Hickin, E.J. Channel Migration and Incision on the Beaton River. *J. Hydraul. Eng.* **1983**, *109*, 327–337. [[CrossRef](#)]
27. Wu, Q.; Ke, L.; Wang, J.; Pavelsky, T.M.; Allen, G.H.; Sheng, Y.; Duan, X.; Zhu, Y.; Wu, J.; Wang, L.; et al. Satellites Reveal Hotspots of Global River Extent Change. *Nat. Commun.* **2023**, *14*, 1587. [[CrossRef](#)] [[PubMed](#)]
28. Boothroyd, R.J.; Williams, R.D.; Hoey, T.B.; Barrett, B.; Prasojo, O.A. Applications of Google Earth Engine in Fluvial Geomorphology for Detecting River Channel Change. *WIREs Water* **2021**, *8*, e21496. [[CrossRef](#)]
29. Witkowski, K. Reconstruction of Nineteenth-Century Channel Patterns of Polish Carpathians Rivers from the Galicia and Bucovina Map (1861–1864). *Remote Sens.* **2021**, *13*, 5147. [[CrossRef](#)]
30. Pavelsky, T.M.; Smith, L.C. RivWidth: A Software Tool for the Calculation of River Widths From Remotely Sensed Imagery. *IEEE Geosci. Remote Sens. Lett.* **2008**, *5*, 70–73. [[CrossRef](#)]
31. Yang, X.; Pavelsky, T.M.; Allen, G.H.; Donchyts, G. RivWidthCloud: An Automated Google Earth Engine Algorithm for River Width Extraction From Remotely Sensed Imagery. *IEEE Geosci. Remote Sens. Lett.* **2020**, *17*, 217–221. [[CrossRef](#)]
32. McFeeters, S.K. The Use of the Normalized Difference Water Index (NDWI) in the Delineation of Open Water Features. *Int. J. Remote Sens.* **1996**, *17*, 1425–1432. [[CrossRef](#)]
33. Xu, H. A study on information extraction of water body with the modified normalized difference water index(MNDWI). *J. Remote Sens.* **2005**, *9*, 589–595.
34. Feyisa, G.L.; Meilby, H.; Fensholt, R.; Proud, S.R. Automated Water Extraction Index: A New Technique for Surface Water Mapping Using Landsat Imagery. *Remote Sens. Environ.* **2014**, *140*, 23–35. [[CrossRef](#)]
35. Fisher, A.; Flood, N.; Danaher, T. Comparing Landsat Water Index Methods for Automated Water Classification in Eastern Australia. *Remote Sens. Environ.* **2016**, *175*, 167–182. [[CrossRef](#)]
36. Wu, T.; Li, M.; Wang, S.; Yang, Y.; Sang, S.; Jia, D. Urban Black-Odor Water Remote Sensing Mapping Based on Shadow Removal: A Case Study in Nanjing. *IEEE J. Sel. Top. Appl. Earth Obs. Remote Sens.* **2021**, *14*, 9584–9596. [[CrossRef](#)]
37. Otsu, N. A Threshold Selection Method from Gray-Level Histograms. *IEEE Trans. Syst. Man Cybern.* **1979**, *9*, 62–66. [[CrossRef](#)]
38. Pan, F.; Xi, X.; Wang, C. A Comparative Study of Water Indices and Image Classification Algorithms for Mapping Inland Surface Water Bodies Using Landsat Imagery. *Remote Sens.* **2020**, *12*, 1611. [[CrossRef](#)]
39. Guo, Q.; Pu, R.; Li, J.; Cheng, J. A Weighted Normalized Difference Water Index for Water Extraction Using Landsat Imagery. *Int. J. Remote Sens.* **2017**, *38*, 5430–5445. [[CrossRef](#)]
40. Zou, Z.; Xiao, X.; Dong, J.; Qin, Y.; Doughty, R.B.; Menarguez, M.A.; Zhang, G.; Wang, J. Divergent Trends of Open-Surface Water Body Area in the Contiguous United States from 1984 to 2016. *Proc. Natl. Acad. Sci. USA* **2018**, *115*, 3810–3815. [[CrossRef](#)]
41. Huete, A.; Didan, K.; Miura, T.; Rodriguez, E.P.; Gao, X.; Ferreira, L.G. Overview of the Radiometric and Biophysical Performance of the MODIS Vegetation Indices. *Remote Sens. Environ.* **2002**, *83*, 195–213. [[CrossRef](#)]

42. Townshend, J.R.G.; Justice, C.O. Analysis of the Dynamics of African Vegetation Using the Normalized Difference Vegetation Index. *Int. J. Remote Sens.* **1986**, *7*, 1435–1445. [[CrossRef](#)]
43. Donchyts, G.; Schellekens, J.; Winsemius, H.; Eisemann, E.; van de Giesen, N. A 30 m Resolution Surface Water Mask Including Estimation of Positional and Thematic Differences Using Landsat 8, SRTM and OpenStreetMap: A Case Study in the Murray-Darling Basin, Australia. *Remote Sens.* **2016**, *8*, 386. [[CrossRef](#)]
44. Cheng, Y.; Xia, J.; Zhou, M.; Deng, S.; Li, D.; Li, Z.; Wan, Z. Recent Variation in Channel Erosion Efficiency of the Lower Yellow River with Different Channel Patterns. *J. Hydrol.* **2022**, *610*, 127962. [[CrossRef](#)]
45. Huang, R.; Li, T.; Zhao, L. Revisiting Functional No-Flow Events in the Lower Yellow River. *Int. J. Sediment. Res.* **2016**, *31*, 351–359. [[CrossRef](#)]
46. Kong, D.; Miao, C.; Wu, J.; Borthwick, A.G.L.; Duan, Q.; Zhang, X. Environmental Impact Assessments of the Xiaolangdi Reservoir on the Most Hyperconcentrated Laden River, Yellow River, China. *Environ. Sci. Pollut. Res.* **2017**, *24*, 4337–4351. [[CrossRef](#)]
47. Hu, C.; Chen, J.; Guo, Q. Shaping and Maintaining a Medium-Sized Main Channel in the Lower Yellow River. *Int. J. Sediment. Res.* **2012**, *27*, 259–270. [[CrossRef](#)]
48. Wang, D.W.; Ji, Z.W.; Chen, J.G. Adjusting the Water-Sediment Matching Relationship to Reduce Sedimentation in the Flow Rate Constraint Reach of the Lower Yellow River, China. *IOP Conf. Ser. Earth Environ. Sci.* **2019**, *344*, 012085. [[CrossRef](#)]
49. Xu, J. A Study of Sediment Delivery by Floods in the Lower Yellow River, China. *Hydrol. Sci. J.* **2003**, *48*, 553–566. [[CrossRef](#)]
50. Yao, B.; Liu, Q. Characteristics and Influencing Factors of Sediment Deposition-Scour in the Sanhuhekou-Toudaoguai Reach of the Upper Yellow River, China. *Int. J. Sediment. Res.* **2018**, *33*, 303–312. [[CrossRef](#)]
51. Kondolf, G.M.; Gao, Y.; Annandale, G.W.; Morris, G.L.; Jiang, E.; Zhang, J.; Cao, Y.; Carling, P.; Fu, K.; Guo, Q.; et al. Sustainable Sediment Management in Reservoirs and Regulated Rivers: Experiences from Five Continents. *Earth's Future* **2014**, *2*, 256–280. [[CrossRef](#)]
52. Wang, H.; Bi, N.; Saito, Y.; Wang, Y.; Sun, X.; Zhang, J.; Yang, Z. Recent Changes in Sediment Delivery by the Huanghe (Yellow River) to the Sea: Causes and Environmental Implications in Its Estuary. *J. Hydrol.* **2010**, *391*, 302–313. [[CrossRef](#)]
53. Wu, X.; Bi, N.; Xu, J.; Nittrouer, J.A.; Yang, Z.; Saito, Y.; Wang, H. Stepwise Morphological Evolution of the Active Yellow River (Huanghe) Delta Lobe (1976–2013): Dominant Roles of Riverine Discharge and Sediment Grain Size. *Geomorphology* **2017**, *292*, 115–127. [[CrossRef](#)]
54. Xia, J.; Wang, Y.; Zhou, M.; Deng, S.; Li, Z.; Wang, Z. Variations in Channel Centerline Migration Rate and Intensity of a Braided Reach in the Lower Yellow River. *Remote Sens.* **2021**, *13*, 1680. [[CrossRef](#)]
55. Hickin, E.J.; Nanson, G.C. The Character of Channel Migration on the Beaton River, Northeast British Columbia, Canada. *Geol. Soc. Am. Bull.* **1975**, *86*, 487. [[CrossRef](#)]
56. Wang, B.; Smith, L.C.; Yang, X.; Pavelsky, T.M.; Altenau, E.H.; Gleason, C.J.; Pietroniro, A.; Rodriguez, E.; Bates, P.D. Remote Sensing of Broad-Scale Controls on Large River Anabranching. *Remote Sens. Environ.* **2022**, *281*, 113243. [[CrossRef](#)]

Disclaimer/Publisher's Note: The statements, opinions and data contained in all publications are solely those of the individual author(s) and contributor(s) and not of MDPI and/or the editor(s). MDPI and/or the editor(s) disclaim responsibility for any injury to people or property resulting from any ideas, methods, instructions or products referred to in the content.